Radial basis function regression of Lagrangian three-dimensional particle tracking data

M. Ratz[1*], S. Sachs[1], J. König[1], M. A. Mendez[2], C. Cierpka[1]

1: Institute of Thermodynamics and Fluid Mechanics, Technische Universität Ilmenau, Germany
2: Environmental and Applied Fluid Mechanics Department, von Karman Institute for Fluid Dynamics, Belgium
*Corresponding author: manuel.ratz@tu-ilmenau.de

Keywords: APTV, microfluidics, radial basis function regression

ABSTRACT

Flow characterization by means of Particle Tracking Velocimetry (PTV) has gained significant importance in recent years. This is especially true in microfluidics, where the limited optical access only allows the use of one c amera. A commonly used technique is the Astigmatism Particle Tracking Velocimetry (APTV), which provides reliable 3D3C velocity measurements. However, for APTV and tracking approaches in general, the resulting data is available on scattered points and usually requires interpolation onto regular grids for further processing. In this work, we test Radial Basis Function (RBF) with the Partition of Unity Method (PUM) for the regression and mesh-free derivative evaluation in dense velocity fields. The RBF-PUM approach is first benchmarked on a synthetic test case against the classic adaptive Gaussian Window interpolation (AGW) and global RBF. Then, we test the RBF-PUM approach on a three-dimensional experimental dataset consisting of 5×10^5 data points in a vortex flow. The results prove that the RBF-PUM allows for accurate regression at accessible computational costs.

1. Introduction

Recently, Lagrangian three-dimensional particle tracking for flow characterization has gained much attention (Kähler et al., 2016). In microfluidics, where the optical access is limited, different techniques based on particle defocusing have been proposed as multi-camera set-ups are usually not feasible. Among these, astigmatism particle tracking velocimetry (APTV) allows the measurement of all three velocity components using only one camera (Cierpka et al. (2010)). As is typical for tracking approaches, the resulting velocity data is scattered due to the nature of the particle tracking and often extends up to 10^6 data points for a sufficient spatial resolution of the observed flow.

For further analysis, such as the computation of derivatives, vortex detection, or pressure computation, classic methods require further data processing (Cierpka & Kähler, 2012) and often interpolating the data onto a regular grid in a postprocessing step. A common approach to achieve this is the adaptive Gaussian window interpolation (AGW, Agüí & Jiménez (1987)). However, the accuracy of interpolating algorithms depends mainly on the number of velocity vectors, the amount

of noise in the measured data, and the interpolating grid's resolution. In general, weighted interpolation suffers in poorly sampled regions that must be interpolated onto fine grids. Furthermore, the subsequent computation of spatial gradients using central differences introduces additional uncertainties and truncation errors.

A way to circumvent these limitations is to use a regression via Radial Basis Functions (RBFs), allowing for deriving a differentiable regression function that enables computing both the velocity fields and their derivatives (see Fornberg & Flyer (2015)) in an arbitrary grid. In recent years, RBF-based regression has also been applied in experimental fluid mechanics to either enhance the resolution of the velocity field or compute spatial derivatives (Casa & Krueger (2013); Karri et al. (2009); Ratz et al. (2021)). Current work includes the meshless computation of the pressure fields (Sperotto et al. (2022a,b)) using RBF regressions that are constrained by differential equations (e.g. solenoidal fields in incompressible flows) and appropriate boundary conditions.

The main limitation of the RBF-based regression is the numerical stability and the high computational cost from large datasets. While the numerical stability can be enforced using appropriate regularization (Larsson et al., 2013), the regression problem leads to large and dense linear systems that have considerable memory demands for realistic 3D datasets. The computational load can be decreased using the Partition of Unity Method (PUM, Larsson et al. (2017)), which consists in splitting the regression of large datasets into smaller portions (partitions). However, depending on the setting of the RBF regression, overlapping regions between partitions can introduce significant errors in the regression. In this work, we analyze the capability of RBF-PUM regression to handle noisy and large datasets and analyze the impact of partitioning on the accuracy of the regression for various RBF parameters. The method is first benchmarked on a synthetic test case, for which the ground truth is available, and then tested on a three-dimensional vortex structure obtained by volumetric APTV measurements in a microchannel. Section 2 briefly introduces the RBF-based regression and its extension to the PUM formulation. Section 3 reports on the testing of the RBF-PUM formulation on a 2D synthetic test case featuring the well-known Lamb-Oseen vortex, while Section 4 reports on the application to the experimental measurements of a 3D vortex flow. Conclusions and outlooks are given in Section 5.

2. The RBF-PUM Approach to Velocity Regression

The RBF-based regression consists in approximating the velocity field as a linear combination of Radial Basis Functions (RBFs). Assuming that a total of n_R RBFs are placed in the measurement domain, the goal of the regression is to find the weights $w_{i,k}$ which map the basis functions onto the velocity field, i.e.:

$$u_i(\mathbf{x}_0) = \sum_{k=1}^{n_R} w_{i,k}\phi_k(\mathbf{x_0}|\mathbf{x_k}, \sigma_\mathbf{k}), \tag{1}$$

where the ϕ_k are the radial basis functions with collocation points $\mathbf{x}_k$ and shape factor σ_k, and u_i is the i-th velocity component sampled on a set of n_S points $\mathbf{x}_0$. In the case of PTV, these points are

scattered randomly over the domain while in the case of classic cross-correlation based velocimetry these are available on a regular grid.

In this work we consider isotropic Gaussians with equal shape ($\sigma_k = \sigma$) as RBFs, that is

$$\phi_k(\mathbf{x_0}|\mathbf{x_k}, \sigma) = \exp\left(-\frac{||\mathbf{x}_0 - \mathbf{x}_k||_2^2}{2\sigma^2}\right), \tag{2}$$

where $||\bullet||_2$ denotes the l_2 norm in the spatial domain ($\mathbb{R}^2$ in planar velocimetry and $\mathbb{R}^3$ in 3D velocimetry). Considering the simplest case with no differential constraints imposed during the regression, the computation of the weights $w_{i,k}$ can be done independently for each of the i-th velocity components. More specifically, the set of weights can be computed solving a linear system arising from a least square problem.

Reshaping the basis functions as columns of a matrix $\mathbf{\Phi}(\mathbf{x}_0) \in \mathbb{R}^{n_S \times n_R}$, collecting the weights $w_{i,k}$ into a column vector $\mathbf{w}_i \in \mathbb{R}^{n_R}$ and the i-th velocity component in $\mathbf{x}_0$ as $\mathbf{u}_i(\mathbf{x}_0) \in \mathbb{R}^{n_S}$, the RBF approximation reads $\mathbf{u}_i(\mathbf{x}_0) = \mathbf{\Phi}(\mathbf{x}_0)\mathbf{w}_i$. The linear system for the least square problem reads:

$$\mathbf{A}\mathbf{w}_i = \mathbf{b}_i \text{ with } \mathbf{A} = \mathbf{\Phi}^T(\mathbf{x}_0)\mathbf{\Phi}(\mathbf{x}_0) \in \mathbb{R}^{n_R \times n_R} \text{ and } \mathbf{b}_i = \mathbf{\Phi}^T(\mathbf{x}_0)\mathbf{u}_i(\mathbf{x}_0) \in \mathbb{R}^{n_R}. \tag{3}$$

Provided that the collocation points $\mathbf{w}_k$ and the shape factors are properly chosen, the matrix $\mathbf{A}$ is (almost) positive definite. Since this condition is hardly met in practice, a gentle regularization $\mathbf{A} \leftarrow \mathbf{A} + \alpha\mathbf{I}$ is usually introduced, with $\alpha \in \mathbb{R}$ and $\mathbf{I}$ the identity matrix of appropriate size. In this work, we consider a regularization based on the infinity norm as suggested by Sperotto et al. (2022a). Then, the system (3) can be solved using a Cholesky decomposition $\mathbf{A} = \mathbf{L}\mathbf{L}^T$, with $\mathbf{L}$ a lower triangular matrix. One should note that only one decomposition is needed since the system matrix is the same for all velocity components.

Once the weights are computed, equation (1) can be used to evaluate the velocity field on any grid (structured or unstructured) and to provide derivatives analytically, by differentiating the RBFs. Given $\mathbf{x} \in \mathbb{R}^{n'_s}$ a new set of points at which the velocity is to be predicted, one has $\mathbf{u}_i(\mathbf{x}) = \mathbf{\Phi}(\mathbf{x})\mathbf{w}_i$, with $\mathbf{\Phi}(\mathbf{x}) \in \mathbb{R}^{n'_s \times n_R}$ the basis matrix evaluated at the new points.

The main limit of the approach is that the matrix $\mathbf{A}$ is dense and thus requires large memory in the case of large datasets. These requirements can be significantly reduced using the Partition of Unity (PUM) approach. The underlying idea of the PUM, as sketched in Fig. 1(a), is to split the regression into smaller partitions and solve it in each partition separately. Denoting the measurement domain as Ω, we define P overlapping patches, active in portions Ω_j, such that $\cup_{j=1}^{P}\Omega_j \supseteq \Omega$. These patches are taken as circles in a 2D domain and spheres in a 3D domain. Similarly to the RBFs, each patch is characterized by its position and radius r. In this work, we control the radius of the patches by an overlap parameter δ. Considering regularly spaced circles on a grid with spacing Δx and denoting as $r^* = \sqrt{2\Delta x^2}$ the minimal radius required to cover the whole domain, we compute the patch's radius as $r = r^*(1 + \delta)$. The overlapping δ is thus an important parameter that is analyzed in the following sections.

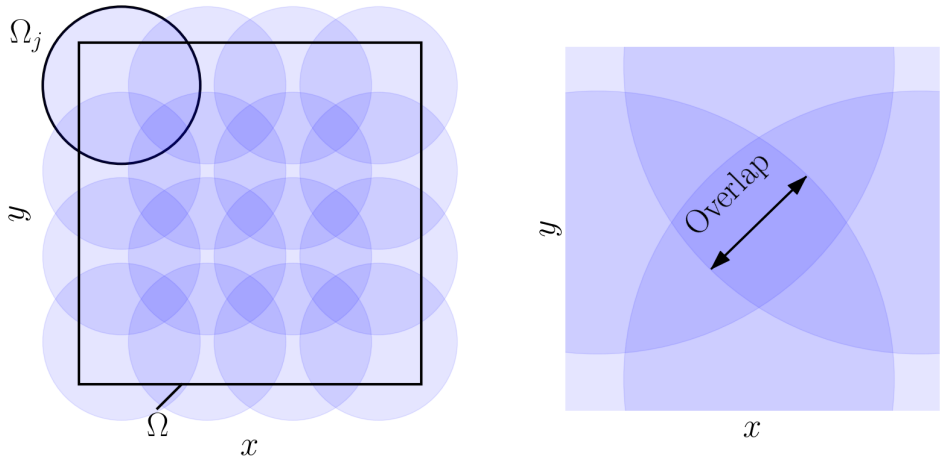

(a) (b)

Figure 1. Illustrations for the PUM. (a) Layout of the circular patches Ω_j in two dimensions to cover the whole measurement domain Ω. (b) Local sketch of the intersection of four circles to explain the patch overlap.

Each patch is identified by a weight function $W_j(\mathbf{x})$ which is approximately unitary in Ω_j and zero outside and it is such that $\sum_{j=1}^{P} W_j(\mathbf{x}) = 1,\ \forall \mathbf{x} \in \mathbf{x}_0$. Applying Shepard's method (Shepard (1968)) of using compactly supported generating function $\varphi_j(\mathbf{x})$, the weight functions are:

$$W_j(\mathbf{x}) = \frac{\varphi_j(\mathbf{x})}{\sum_{m=1}^{P} \varphi_m(\mathbf{x})}. \tag{4}$$

An example of compactly supported generating function is the C^2 Wendland function (Wendland, 1995) $\varphi(r) = (4r+1)(1-r^4)_+$, where the subscript $_+$ denotes that only the positive part is taken, i.e. $(x)_+ = x$ if $x > 1$ and 0 otherwise.

Once the regression in each patch is computed, the regression of the global velocity field is taken as a weighted combination of the individual fields, i.e. :

$$u_i(\mathbf{x}) = \sum_{j=1}^{P} W_j(\mathbf{x}) u_{i,j}(\mathbf{x}), \tag{5}$$

where $u_{i,j}(\mathbf{x})$ is the regression of the component i in the patch j. In practice, we require an overlap parameter $\delta > 0$ to ensure all points are resolved on the new grid $\mathbf{x}$. Because the approach acts as an interpolant in the overlapping regions, these represent a critical area for the regression, especially if these occur in regions where the velocity field features large gradients.

3. Synthetic Test Case

We consider a classic benchmark problem, namely the 2D Lamb-Oseen vortex in a square domain of $[-250, 250] \times [-250, 250]$ px. In radial coordinates, denoting with r the (radial) distance in pixels

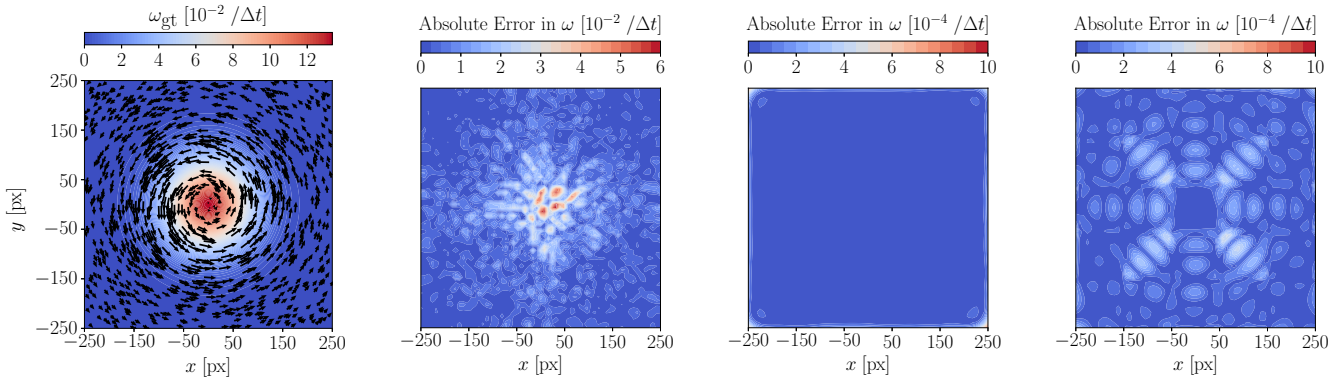

(a) (b) $\omega_{\text{err}} = 27.3\%$ (c) $\omega_{\text{err}} = 0.19\%$ (d) $\omega_{\text{err}} = 0.34\%$

Figure 2. Results for the Lamb Oseen vortex with no noise and 10^4 points. (a) Ground truth of the vorticity with the scattered data. Local errors in vorticity after the regression for the (b) AGW (c) RBF global (d) RBF-PUM. The subcaptions show the reconstruction error.

from the image center, the angular velocity is set to $v_\theta = (1 - e^{-r^2/a})/(r + \varepsilon)$, with $\varepsilon = 10^{-10}$ and $a = 10^3$. This yields a maximum displacement, between two consecutive snapshots, of 3.2 px at $r = 112.2$ px. A total of 10^4 sampling points are considered, randomly scattered through the image to simulate seeding particles. Figure 2(a) shows the an example snapshot from the vorticity field with a quiver plot of the velocity. Here, only one data point only every ten is plotted for visualization purposes.

We compare the performance of the RBF-PUM to a global RBF regression and an AGW interpolation. We define the reconstruction error ω_{err} of the vorticity as:

$$\omega_{\text{err}} = \frac{||\omega_{\text{gt}}(\mathbf{x_g}) - \omega_{\text{reg}}(\mathbf{x_g})||_2}{||\omega_{\text{gt}}(\mathbf{x_g})||_2}, \tag{6}$$

where $||\bullet||_2$ is the l_2 norm of a vector, $\mathbf{x_g}$ is a structured grid of 63×63 points, ω_{gt} the analytical vorticity field of the flow and ω_{reg} the regressed vorticity field from either of the interpolation methods.

For the AGW interpolation, we choose regression regions of size 40×40 px with an overlap of 80%. We apply a relatively strong filter by removing vectors in a regression region whose velocity components differ by more than the square root of two standard deviations from the median in the given regression region, i.e. $\sqrt{2\ \text{Var}(u_i)}$, as is usually done (Sachs, Cierpka, & König, 2022). The choice of collocation points for the RBF regression is not straightforward as many methods exist to determine the position and shape parameter for each RBF. However, one approach often taken is to place collocation points randomly and then choose the shape parameter based on the average distance between them (Schneiders & Scarano, 2016). However, this choice of the shape parameter does not consider the physics of the flow. For example, a flow with a relatively low spatial frequency tolerates larger shape parameters because there is no need to represent spikes or sharp gradients. In this work, we heuristically chose the shape parameter equal to twice the grid

spacing h. Using a total number of 1250 collocation points, this yields $\sigma = 2\ h \approx 63$ px. For the RBF-PUM, we choose a total number of 25 patches. The overlap parameter δ is 0.2 as proposed in the initial work (Larsson et al., 2017).

The local absolute errors for the AGW, global RBF and RBF-PUM are shown in Fig. 2(b), 2(c) and 2(d) respectively. The subcaptions show the reconstruction error in each case. We also want to emphasize the scale of the colorbars showing the error. For the AGW, the absolute error is two orders of magnitude larger than in both cases of the RBFs. Moreover, the AGW error is larger in regions of large velocity gradients, i.e. in the center of the domain, while the error in both RBF is more uniform and mainly influenced by the domain's boundaries.

This is particularly evident in the RBF-PUM, as the footprint of the PUM's patches is visible in the error landscape. Increasing the number of patches does not yield appreciable changes in the global error, which remains comparable to the global RBF.

In terms of computational cost, the RBF regression requires the solution of a linear system of size $n_R \times n_R$ which is assembled at a cost of $n_R^2 n_S$. In the global RBF, we have $n_R = 1250$ and $n_S = 10^4$ while in the PUM-RBF we have $P = 25$ systems of size $n_R = 110$ and $n_P = 874$. On an Intel i7-4790K CPU with $4\,\mathrm{GHz}$, the computation time on a python platform was $1.8\,\mathrm{s}$ for the global RBF and $0.35\,\mathrm{s}$ for RBF-PUM. Going to higher seeding concentrations rapidly increases this difference. In these cases, only the RBF-PUM can be applied and the results on clean data show that it yields very comparable results to the global RBF regression.

Another aspect to consider is that experimental data is inherently noisy. While noise has been considered in the past (Li et al., 2021), it was only for the case of lower seeding concentrations and PTV setups, which have an uncertainty in the particle center location below 0.1 px. In a recent investigation of Barnkob et al. (2021), the uncertainty for the in plane location was estimated to be below 0.7 px for noisy and densely seeded images. Although it was not reported to what extent this value depends on the repositioning accuracy of the stage used by the authors, we take this value as a lower bound for the following investigation. Assuming a displacement between two frames to be ≈ 20 px, we consider random Gaussian noise with a standard deviation of 5% of the corresponding velocity. We also add random spikes into the velocity field, simulating the effects of mismatched particles. For this, 0.5% of the data points have their velocity multiplied with a factor of 10 and random noise taken from a uniform distribution. As we now want to investigate the effect of even larger data densities, we take a total of 5×10^4 randomly placed data points. We apply a small preprocessing step by removing sharp outliers with a normalized median filter (Westerweel & Scarano, 2005) that has been extended to PTV data (Sachs, Baloochi, et al., 2022) to remove some of the spikes and noise. For the given case, 495 of the data points were removed in this way. Nevertheless, not all of them contain spikes.

To see how the RBF regression performs in this case Fig. 3(a) shows the reconstruction error for different combinations of overlap $\delta \in [0.1, 0.9]$ and shape parameter $\sigma \in [35, 125]$ px. The number of collocation points and patches is the same as for the case without noise. As we can see, the

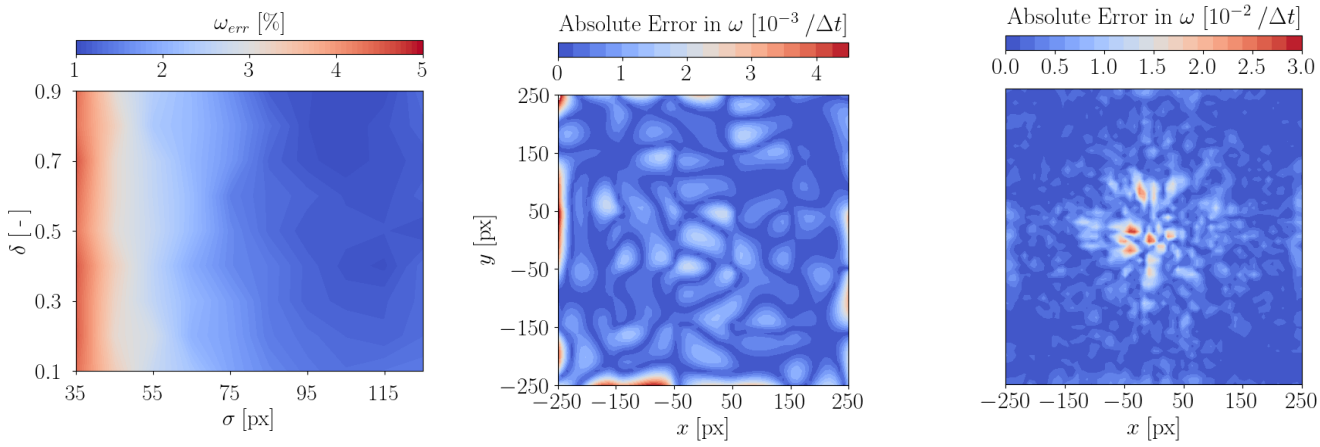

(a) (b) $\omega_{\text{err}} = 2.77\%$ (c) $\omega_{\text{err}} = 12.34\%$

Figure 3. Test Case of the Lamb-Oseen vortex with gauss noise, spikes and 5×10^4 data points. (a) Overlap over sigma showing that flatter RBFs are prefered. Absolute Error in the vorticity for the RBF-PUM and AGW (c).

error has increased by an order of magnitude compared to the case without noise in Fig. 2(d). The figure shows that larger shape parameters are beneficial for noisy data. This is not surprising, as flatter Gaussians lead to a higher degree of smoothing. Furthermore, increasing the overlap only results in minor improvements, regardless of the shape parameters. One reason for this could be the aforementioned smoothing produced by (4) that occurs for large overlaps. However, the benefit is much smaller than compared to varying the shape parameter. Larger overlaps also increase the computational cost, e.g. for $\delta = 0.1$ and 0.9, the regression time is $0.44\,\text{s}$ and $3.22\,\text{s}$, respectively. While this is still relatively short, the computational cost increases for larger datasets in three dimensions and if more collocation points are chosen for more complex flows.

Using this knowledge, we compare the performance of RBF-PUM with $\delta = 0.3$ and $\sigma = 105$ px with AGW. The results are shown in Figure 3(b) and 3(c), the subcaptions show the reconstruction error. The RBF-PUM still performs better than the AGW with a reconstruction error of $\omega_{\text{err}} = 2.77\%$ compared to 12.34%. However, the difference is not as significant as for the case without noise. It is worth mentioning that the AGW performs better than in the case without noise, which is to be expected as the number of points also increased. This results in better averaging in the regression regions, and noise is removed very well due to the inbuilt filtering of the algorithm. Nevertheless, RBF-PUM has a smaller error and allows computing gradients analytically.

4. Experimental Data

The RBF-PUM is now applied to real APTV measurements and compared to the AGW. The configuration of interest is a microchannel made of polydimethylsiloxane (PDMS) with a rectangular cross-section of about $500\,\mu\text{m}$ in width and height. A sketch is shown in Fig. 4. The channel is placed on 128° YX $LiNbO_3$ on which two interdigital transducers (IDTs) are deposited. These

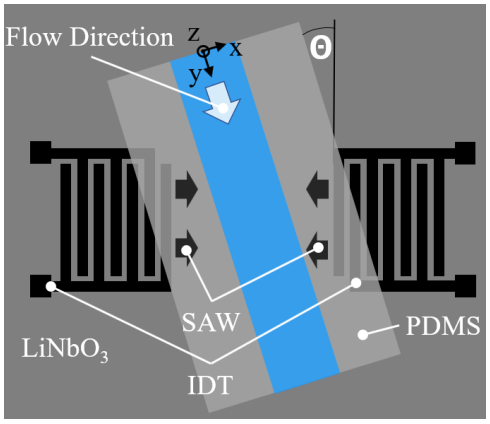

Figure 4. Sketch showing the experimental setup of the channel that is tilted by Θ with respect to the IDTs. Counter-propagating surface acoustic waves are excited on the piezoelectric substrate of $LiNbO_3$.

are used to excite two counter-propagating surface acoustic waves (SAWs), which superimpose to form a standing wave field within the fluid. Due to the viscous damping of the radiated bulk acoustic waves, a stationary vortex is induced. A detailed explanation of the involved physical mechanisms, the electronic devices and the experimental setup is given in (Sachs, Cierpka, & König, 2022; Sachs, Baloochi, et al., 2022). Here, the channel's position is slightly modified to include a tilting angle of $\Theta = 6°$ between the IDTs and the channel. The SAWs had a wavelength of $90\,\mu\mathrm{m}$ and the applied power (PowerSAW generator, BelektroniG GmbH) was set to $\approx 29.5\,\mathrm{mW}$. In total, 3.8×10^5 valid vectors are found inside the measurement volume, which covered the whole channel cross-section and about $800\,\mu\mathrm{m}$ in the main flow direction.

For the AGW, cube-shaped regression regions with a side length of $40\,\mu\mathrm{m}$ and an overlap of $50\,\%$ are chosen, yielding a grid of $23 \times 37 \times 26$ points along x, y, z. For the RBF-PUM, the results from Section 3 are taken into consideration. We placed 2600 collocation points in our measurement volume and the RBFs cover a wide domain with $\sigma = 125\,\mu\mathrm{m}$. The number of spheres is $5 \times 7 \times 5$ along x, y, z and the overlap is set to $\delta = 0.2$.

Fig. 5(a) shows a vertical slice of the $y-$component of the velocity field, obtained by sampling valid velocity vectors in the region $y \in [405, 415]\,\mu\mathrm{m}$. The contourmap shows noise from the experiments and a lack of data on the channel cross-section's top right and left corners. Here, no valid vectors were found.

Fig. 5(b) and 5(c) shows the same velocity component after reconstruction at $y = 410\,\mu\mathrm{m}$ for the RBF-PUM and AGW, respectively. The RBF-PUM yields a smooth velocity field that appears symmetric whereas the AGW has some issues, especially towards the top right corner. The lack of data points in this region leads to a velocity field that appears to be still noisy.

The resulting vortex is illustrated in Fig. 6. The vortices are highlighted by isosurfaces of the Q-field (Hunt et al., 1988) with a threshold of $2\,\mathrm{s}^{-2}$ and streamlines, colored according to the velocity component v in main flow direction. The derivatives for the AGW are calculated with central differences and analytically for the RBF-PUM. The results obtained with RBF-PUM are shown on

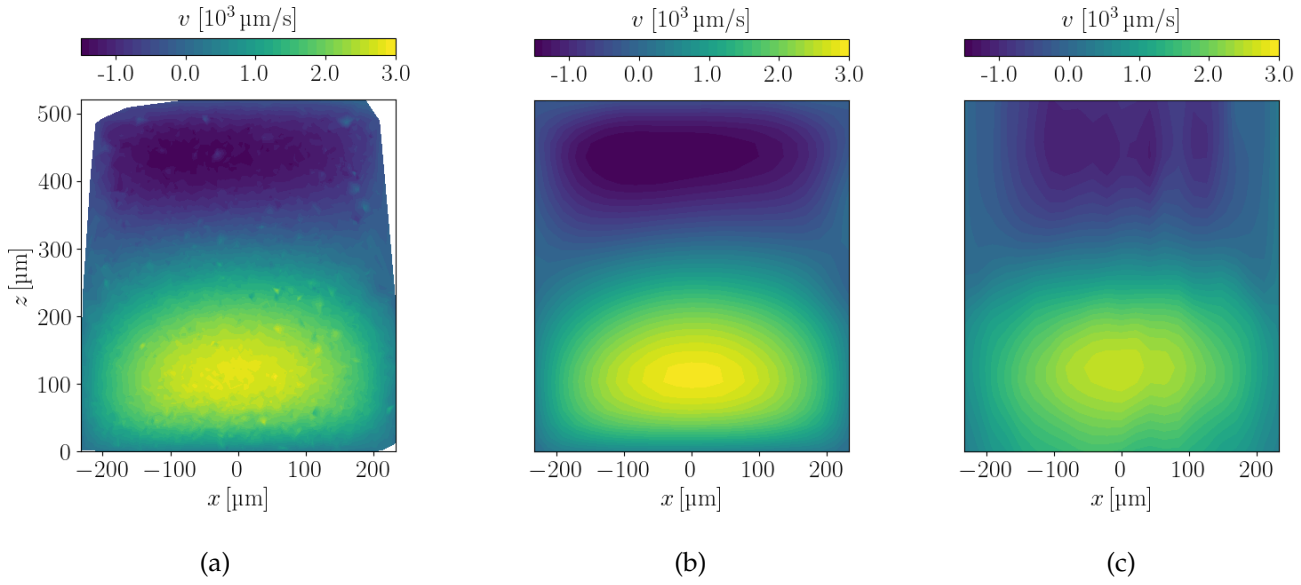

Figure 5. Slices of the velocity field in y-direction. Fig (a) Scattered data taken from $y \in [405, 415]$ µm. Fig (b) and (c) Velocity field after the regression at $y = 410$ µm for the RBF-PUM and AGW respectively.

the left-hand side and with AGW on the right-hand side, each from a three-dimensional view in the top row and a top-down view in the bottom row. The colorbar of the streamlines is identical for each case and chosen with manual thresholds of $-1500\,\mu\mathrm{m\,s^{-1}}$ and $3000\,\mu\mathrm{m\,s^{-1}}$. The resulting isosurfaces look very similar for both regression methods, with small outliers present towards the walls in both cases. For the AGW, this can be traced back to a lack of points in these regions, and for the RBF-PUM the lack of boundary conditions. Furthermore, more streamlines are retained for the RBF regression at the same seeding concentration, which gives a more detailed representation of the flow field. Nevertheless, both regression methods clearly show the tilt of the vortex due to the angle between the IDTs and the channel. This effect can also be seen in the tilt of the streamlines.

5. Conclusions and Perspectives

Radial Basis Function regression has been successfully applied to large, three-dimensional data. To limit the computational cost of a global regression, the Partition of Unity Method has been used. The results of a synthetic test case show that both methods yield similar errors and vastly outperform the adaptive Gaussian window interpolation. Furthermore, RBF-based methods have the key advantage of providing an analytical expression of the velocity field. This allows the analytical computation of spatial derivatives.

However, strong noise reduces the performance of the RBF-PUM. Nevertheless, with the correct choice of the hyperparameters, the RBF still outperforms the AGW. Both methods were then applied to a three-dimensional vortex and showed a good agreement. The RBF-based methods can further be improved by including boundary conditions such as the no-slip condition.

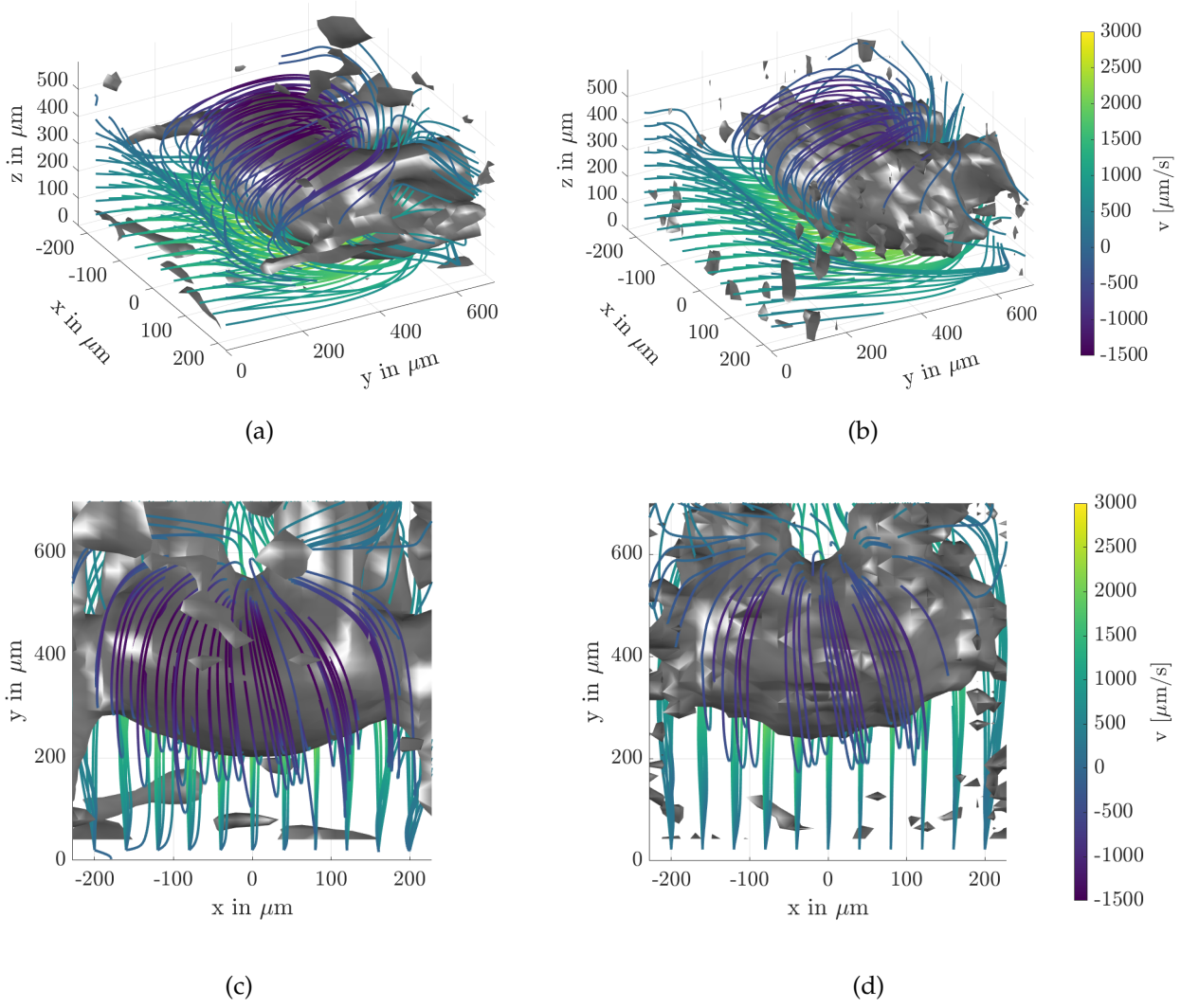

Figure 6. Three-dimensional flow field visualization of the SAW-induced vortex using streamlines and isosurfaces (grey) of the Q-field with a threshold of $2\,\mathrm{s}^{-2}$. Side view of the vortex obtained from the RBF regression (a) and the AGW interpolation (b). Top-down view of the vortex for the RBF regression (a) and AGW interpolation (b). The colorbar is the same for both interpolation methods.

Acknowledgements

The authors thank the Deutsche Forschungsgemeinschaft (DFG) for financial support within the priority program SPP2045 "MehrDimPart" (CI 185/8-1). Furthermore, support by the Center of Micro- and Nanotechnologies (ZMN), a DFG-funded core facility of TU Ilmenau, is gratefully acknowledged.

References

Agüí, J. C., & Jiménez, J. (1987). On the performance of particle tracking. *Journal of Fluid Mechanics*, *185*, 447–468.

Barnkob, R., Cierpka, C., Chen, M., Sachs, S., Mäder, P., & Rossi, M. (2021). Defocus particle tracking: a comparison of methods based on model functions, cross-correlation, and neural networks. *Measurement Science and Technology*, *32*, 094011.

Casa, L., & Krueger, P. (2013). Radial basis function interpolation of unstructured, three-dimensional, volumetric particle tracking velocimetry data. *Measurement Science and Technology*, *24*, 065304.

Cierpka, C., & Kähler, C. J. (2012). Cross-correlation or tracking-comparison and discussion. In *16th International Symposium on Applications of Laser and Imaging Techniques to Fluid Mechanics, Lisbon, Portugal.*

Cierpka, C., Rossi, M., Segura, R., & Kähler, C. J. (2010). On the calibration of astigmatism particle tracking velocimetry for microflows. *Measurement Science and Technology*, *22*, 015401.

Fornberg, B., & Flyer, N. (2015). Solving PDEs with radial basis functions. *Acta Numerica*, *24*, 215–258.

Hunt, J., Wray, A., & Moin, P. (1988). Eddies, streams, and convergence zones in turbulent flows. In *Studying turbulence using numerical simulation databases, 2. Proceedings of the 1988 Summer Program, Stanford, California, USA.*

Kähler, C. J., Astarita, T., Vlachos, P. P., Sakakibara, J., Hain, R., Discetti, S., … Cierpka, C. (2016). Main results of the 4th international piv challenge. *Experiments in Fluids*, *57*, 1-71.

Karri, S., Charonko, J., & Vlachos, P. (2009). Robust wall gradient estimation using radial basis functions and proper orthogonal decomposition (POD) for particle image velocimetry (PIV) measured fields. *Measurement Science and Technology*, *20*, 045401.

Larsson, E., Lehto, E., Heryudono, A., & Fornberg, B. (2013). Stable computation of differentiation matrices and scattered node stencils based on Gaussian radial basis functions. *SIAM Journal on Scientific Computing*, *35*, 2096–2119.

Larsson, E., Shcherbakov, V., & Heryudono, A. (2017). A least squares radial basis function partition of unity method for solving PDEs. *SIAM Journal on Scientific Computing*, *39*, 2538–2563.

Li, L., Sellappan, P., Schmid, P., Hickey, J.-P., Cattafesta, L., & Pan, Z. (2021). Lagrangian strain- and rotation-rate tensor evaluation based on multi-pulse particle tracking velocimetry (MPTV) and radial basis functions (RBFs). *14th International Symposium on Particle Image Velocimetry*, *1*.

Ratz, M., Fiorini, D., Alessia, S., Cierpka, C., & Mendez, M. A. (2021). Time resolved PIV of the flow field underneath an accelerating meniscus. *15th International Symposium on Particle Image Velocimetry*, *1*.

Sachs, S., Baloochi, M., Cierpka, C., & König, J. (2022, 04). On the acoustically induced fluid flow in particle separation systems employing standing surface acoustic waves - part i. *Lab on a chip*. doi:

Sachs, S., Cierpka, C., & König, J. (2022). On the acoustically induced fluid flow in particle separation systems employing standing surface acoustic waves - part II. *Lab on a chip*.

Schneiders, J. F. G., & Scarano, F. (2016). Dense velocity reconstruction from tomographic ptv with material derivatives. *Experiments in Fluids*, *57*, 1-22.

Shepard, D. (1968). A two-dimensional interpolation function for irregularly-spaced data. In *Proceedings of the 1968 23rd ACM national conference* (p. 517–524). New York, NY, USA: Association for Computing Machinery.

Sperotto, P., Pieraccini, S., & Mendez, M. (2022a). A meshless method to compute pressure fields from image velocimetry. *Measurement Science and Technology*.

Sperotto, P., Pieraccini, S., & Mendez, M. (2022b). A RANS approach to the meshless computation of pressure fields from image velocimetry. In *20th International Symposium on Applications of Laser and Imaging Techniques to Fluid Mechanics, Lisbon, Portugal.*

Wendland, H. (1995). Piecewise polynomial, positive definite and compactly supported radial functions of minimal degree. *Advances in Computational Mathematics*, *4*, 389-396.

Westerweel, J., & Scarano, F. (2005). Universal outlier detection for PIV data. *Experiments in Fluids*, *39*, 1096–1100.